Mind the Gap – Imaging Buried Interfaces in Twisted Oxide Moirés

Harikrishnan KP[1,], Xin Wei[2,3], Chia-Hao Lee[1], Dasol Yoon[4], Yonghun Lee[2,5], Kevin J. Crust[2,3], Yu-Tsun Shao[1,6], Ruijuan Xu[2,5,7], Jong-Hoon Kang[8,9,10], Ce Liang[11], Jiwoong Park[8,11,12], Harold Y. Hwang[2,5], David A. Muller[1,13,*]*

[1.] *School of Applied and Engineering Physics, Cornell University, Ithaca, NY 14853, USA.*

[2.] *Stanford Institute for Materials and Energy Sciences, SLAC National Accelerator Laboratory, Menlo Park, CA 94025, USA.*

[3.] *Department of Physics, Stanford University, Stanford, CA 94305, USA.*

[4.] *Department of Materials Science and Engineering, Cornell University, Ithaca, NY 14853, USA.*

[5.] *Department of Applied Physics, Stanford University, Stanford, CA 94305, USA.*

[6.] *Mork Family Department of Chemical Engineering and Materials Science, University of Southern California, Los Angeles, CA 90089, USA.*

[7.] *Department of Materials Science and Engineering, North Carolina State University, Raleigh, NC 27695, USA.*

[8.] *Department of Chemistry, University of Chicago, Chicago, IL 60637, USA.*

[9.] *Center for Van der Waals Quantum Solids, Institute for Basic Science (IBS), Pohang 37673, Korea.*

[10.] *Department of Materials Science and Engineering, Pohang University of Science and Technology (POSTECH), Pohang 37673, Korea.*

[11.] *Pritzker School of Molecular Engineering, University of Chicago, IL 60637, USA.*

[12.] *James Franck Institute, University of Chicago, Chicago, IL 60637, USA.*

[13.] *Kavli Institute at Cornell for Nanoscale Science, Cornell University, Ithaca, NY 14853, USA.*

[*] *Corresponding Authors: E-mail: hk944@cornell.edu, david.a.muller@cornell.edu*

Abstract

The ability to tune electronic structure in twisted stacks of layered, two-dimensional (2D) materials has motivated the exploration of similar moiré physics with stacks of twisted oxide membranes. Due to the intrinsic three-dimensional (3D) nature of bonding in many oxides, achieving atomic-level coupling is significantly more challenging than in 2D van der Waals materials. Although clean interfaces with atomic level proximity have been demonstrated in ceramic bicrystals using high-temperature and high-pressure processing to facilitate atomic diffusion that flattens rough interfaces, such conditions are not readily accessible when bonding oxide membranes. This study shows how topographic mismatch due to surface roughness of the membranes can restrict atomic-scale proximity at the interface to isolated patches even after obvious issues of contaminants and amorphous interlayers are eliminated. In hybrid interfaces between a chemically inert 2D material and an oxide membrane, the reduced ability of the 2D material to conform to the membrane's step-terrace topography also limits atomic-scale contact. In all these material systems, the interface morphology is best characterized using cross-sectional imaging and is necessary to corroborate investigations of interlayer coupling. When imaging the bicrystal in projection, conventional

through-focal imaging is found to be relatively insensitive to the buried interface, whereas electron ptychography reliably resolves structural variations on the order of a nanometer. These findings highlight interface roughness as a key challenge for the field of oxide twistronics and emphasizes the need for reliable characterization methods.

1. Introduction

Propelled by the experimental discovery of superconductivity in twisted bilayer graphene[1], the last few years have witnessed tremendous interest in the field of "twistronics" where the twist angle between 2D materials in a van der Waals heterostructure is tuned to control electronic correlations in the emergent moiré superlattice[2–5]. In addition to superconductivity, the twist angle tuning parameter has also led to the demonstration of other correlated electronic states like Mott insulators, Wigner crystals, Chern insulators, and orbital magnetism in these moiré materials constructed with 2D materials as building blocks[6–11]. Recent developments in the growth and manipulation of free-standing oxide membranes have opened up the opportunity to create and explore similar moiré physics in twisted stacks of oxides[12–18]. However, due to the three-dimensional nature of bonding in many oxide materials, achieving atomic scale interlayer coupling is more challenging than in 2D materials. The presence of dangling bonds at the surfaces of oxides can result in surface reconstructions and adsorption, often resulting in a substantial dead layer between the two membranes in a stacked bilayer. Due to the possibility of such an interfacial dead layer from fabrication, investigation of interlayer coupling in stacked bilayer oxides requires careful examination of the close structural proximity (interfacial gap ~ 5 Å) of the two layers at the interface. Even when interfacial dead layers are eliminated through optimization of the assembly process, here we observe that surface roughness of the membranes hinders interfacial coupling over extended areas, limiting atomic-scale proximity to isolated patches. Interfacial coupling over extended length-scales have been achieved in fused ceramic bicrystals[19–21] with atomically sharp interfaces between different oxide single crystals or thin films, where high temperatures are required to facilitate atomic flow and bridge the interfacial gap. Reproducing the same level of control with membranes is a central challenge for oxide twistronics, and a method to assess interface quality would greatly aid progress in the field.

Due to the nanometer length-scale of the moiré lattice and spatial inhomogeneities in a stacked bilayer sample, scanning transmission electron microscopy (STEM) is well-suited for structural characterization of these stacked heterostructures. The typical approach for 3D imaging using conventional STEM techniques involves acquiring an optical depth-sectioning series (through-focal series) of images by varying the focal point of the probe to different positions in the depth direction. However, this approach is dose-inefficient, and can produce inaccurate results for crystalline samples due to strong channeling effects of the electron beam[22,23]. For these reasons, we show that through-focal imaging with conventional STEM methods is inadequate for detecting and probing dead layers, if present at the interface between stacked membranes. Instead, we apply a new 3D imaging technique - multislice electron ptychography (MEP)[24,25],

that enables the accurate reconstruction of the 3D specimen potential[26–32] with a typical depth resolution of 2-3 nm. We demonstrate that MEP can detect the presence or absence of strain fields in the membranes as well as interfacial dead layers in stacked bilayers and explore its sensitivity and depth resolution. To demonstrate atomic-abruptness, cross-sectional images are still needed. By comparison with cross-sectional images, we also identify ~10% systematic underestimation of sample extent in the depth direction in MEP reconstructions, arising from the use of a purely elastic scattering model that neglects electron-phonon interactions.

2. Retrieving 3D information using the Parallax Effect

MEP uses the same experimental setup as conventional STEM imaging where a convergent electron beam is scanned across the sample, but now with the momentum-resolved scattering information recorded in the far-field using a pixelated detector for each scan position as shown in Fig. 1(a). At the convergence angles typically used for atomic-resolution imaging, the diffraction pattern consists of overlapping disks, with phase information encoded in their overlap region from the interference of scattered wavefunctions. As the probe position is shifted, this phase information evolves according to the Fourier shift theorem, allowing its extraction from heavily oversampled scans that offer sufficient redundancy for a reliable reconstruction. With the knowledge of a forward model that describes the scattering physics, the specimen potential is determined by iterative algorithms that solve the phase problem with optimization techniques. We use the well-established multislice algorithm[33] as our forward model, where the sample potential is divided into a series of slices along the beam direction, and the electron wavefunction sequentially scatters off each slice with free-space propagation between the slices.

As MEP solves the inverse multislice imaging problem, the reconstruction contains multiple slices of the sample potential, reflecting the changes in sample structure along the depth direction. The depth-resolved information is extracted from a single dataset, without the need for a through-focal series and instead relies on the parallax effect[26,34] summarized in Fig. 1. For illustration purposes, we use an array of atoms shaped like a duck and a cloud as two scattering species, with the former located closer to the focal point of the probe. The diffraction patterns calculated for three different probe positions indicated in the schematic are shown in Fig. 1(b-d) and show the imprint of the scattering from the two objects as a shadow image in the bright field disk. The shadow image of the duck moves faster across the bright field disk with shifts in probe position in comparison to the cloud. This observation is explained by the parallax effect, which causes shadow images of objects located closer to the focal point of the probe to move faster in the diffraction plane as the probe is scanned. Hence, depth information is encoded in diffraction patterns in the form of differences in distance moved by the scattering imprints from different objects for a fixed shift in probe position. This information is utilized in MEP reconstructions to achieve depth resolution.

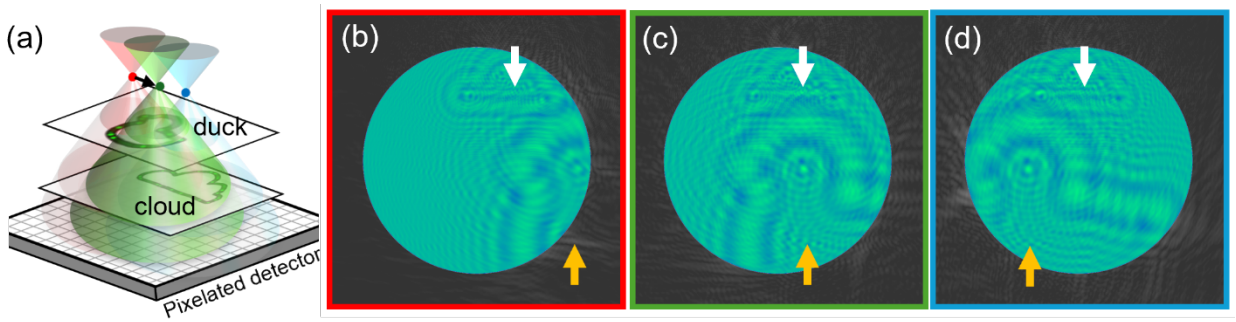

Figure 1. How depth information is encoded in ptychographic data. *(a) Schematic of the experimental setup for ptychography where a converged beam of electrons scatters off the sample and a pixelated detector collects the diffraction pattern in the far-field. The sample here is an array of atoms forming the outline of a duck and a cloud, spatially separated along the beam direction. The diffraction patterns corresponding to three different probe positions indicated with red, green and blue dots are shown in (b-d). Due to the parallax effect, the shadow image of the duck which is closer to the focal point of the probe moves faster across the bright field disk compared to the cloud. The white and yellow arrows in (b-d) point to the center of the cloud and the eye of the duck respectively and acts as a guide to the eye for tracking their movement across the bright field disk. Hence, depth information is encoded in diffraction patterns in the form of differences in distance moved by the scattering imprints from different objects for a fixed shift in probe position.*

3. Buried interfaces in twisted oxide stacks

We use MEP for the three-dimensional imaging of oxide membrane heterostructures and compare the results with depth sectioning using conventional high-angle annular dark field (HAADF) imaging. We show that plan-view through-focal imaging can fail to detect an interfacial dead layer due to channeling and projection artifacts. While MEP is sensitive to the dead layer under certain conditions as demonstrated below, cross-sectional imaging is still essential for examining the interface and the potential for interlayer coupling.

We use an example of a stacked bilayer of $SrTiO_3$ (Sample 1), assembled with typical protocols used in literature[12,13,35]. A cross-sectional HAADF image of the stacked bilayer of $SrTiO_3$ with a 9-degree twist between the two membranes is shown in Fig. 2(a), showing a dead layer that appears as a "gap" of ~1.5 nm between the two membranes, similar to prior observations[16,35,36]. Elemental identification with energy-dispersive X-ray (EDX) spectroscopy indicates that the gap region is comprised of organic materials as well as oxides of residual elements from the sacrificial layer used during growth of the membranes (Supplementary Fig. 1). In order to explore if the dead layer can be removed by optimizing assembly and with higher temperature annealing, we prepared another $SrTiO_3$ bilayer sample - Sample 2 (details of preparation in Methods section). Cross-sectional HAADF imaging of Sample 2 reveals isolated patches where the two membranes are in close proximity, closer to bridging the interfacial gap, as shown in Fig.

2(b). Such atomically proximal regions occur only in patches due to the surface roughness of the membranes and their inability to conform to the surface step-terrace structure. In Supplementary Fig. 2, we show how the step terraces on the membrane surfaces result in a wide range (0.7 nm – 2.2 nm) for the extent of the interfacial gap, even within a small field of view (~85 nm). EDX elemental profiles across the interface of Sample 2 are also shown in Supplementary Fig. 3.

These findings indicate that while an interface with atomic-level proximity can be achieved over atomic length scales, replication over an extended area requires a clean and smooth surface termination with well-separated terraces for both membranes. While these results show that there are both challenges and opportunities to fabricate atomically precise oxide bilayers, we focus here on Sample 1 and the imaging challenges of a gapped interface.

Even in the presence of a considerable interfacial separation, the stacked bilayer will still produce a moiré pattern when imaged top-down (plan-view) in projection as shown in Fig. 2(c, d). The HAADF-STEM projection image in Fig. 2(c) is obtained by summing over all the images acquired through an optical depth-sectioning series, while Fig. 2(d) shows the projected ptychographic image obtained by summing up all slices from a MEP reconstruction. Although the projection images with the 2 methods shown in Fig. 2(c, d) have the same sample orientation and cover the same spatial extent, they appear visually distinct due to the different dependence of HAADF and multislice ptychographic image intensity on the atomic number (Z) of the scattering atoms. The moiré pattern in the HAADF image also appears tilted relative to that in the MEP image, as the through-focal HAADF series predominantly captures contrast from the upper membrane, whereas the MEP image captures contrast uniformly from both layers.

We additionally note that rescaling the HAADF moiré pattern in both lateral dimensions by a factor of $1/\sqrt{2}$ followed by a 45° rotation makes the resulting pattern visually identical to the moiré pattern obtained with MEP, as shown in Supplementary Fig. 4. The explanation for this connection, as well as schematic models differentiating the AA and AB stacked regions in the moiré pattern, are shown in Supplementary Figs. 5, 6.

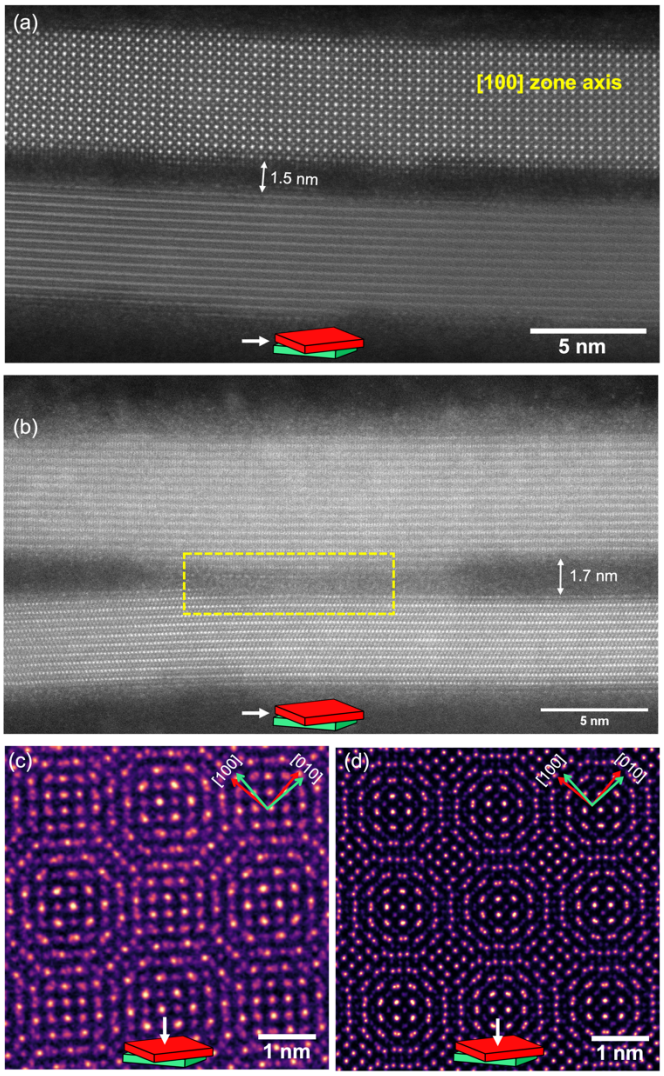

Figure 2. Cross-sectional and plan-view imaging of the stacked bilayer. *(a) Cross-sectional HAADF image of stacked bilayer $SrTiO_3$ membranes (Sample 1) showing a dead layer of ~1.5 nm at the interface, suggesting negligible coherent interlayer coupling. (b) Cross-sectional HAADF image of Sample 2 showing an isolated patch labelled with a yellow dotted box, where atomic planes close the interfacial gap. The presence of such patches indicate that atomically proximal interfaces are achievable but eliminating surface roughness is important for getting clean interfaces over extended areas. (c, d) Plan-view projection images of the Sample 1 projected through sample depth, obtained by summing up (c) a through-focal series of HAADF images and (d) all slices in a MEP reconstruction. Both images show the moiré structure arising from the twist angle (9°) between the two membranes. The directions corresponding to the cubic axes for the two membranes are labelled on the top right. Although both images have the same sample orientation and field of view, the HAADF image appears tilted compared to the MEP image as HAADF imaging picks up most contrast from the upper layer, while the MEP image captures contrast uniformly from both layers.*

Further, we compare the 3D volumetric data obtained using through-focal HAADF series and MEP in Fig. 3, which shows the 3D volume rendering of the twisted bilayer structure when viewed along three orthogonal axes. Prior work has shown that the contrast of HAADF imaging is highly depth-sensitive due to electron beam channeling, with optimal contrast when the probe is focused near the top of the sample, and a gradual decline in contrast as the probe is focused deeper into the sample[37]. Such depth-dependent contrast and limited depth resolution of through-focal HAADF imaging makes it very difficult to detect the gap between the two layers, as shown in Fig. 3(a). Similar channeling artifacts are also observed in integrated Differential Phase Contrast (iDPC) imaging as shown in Supplementary Fig. 7.

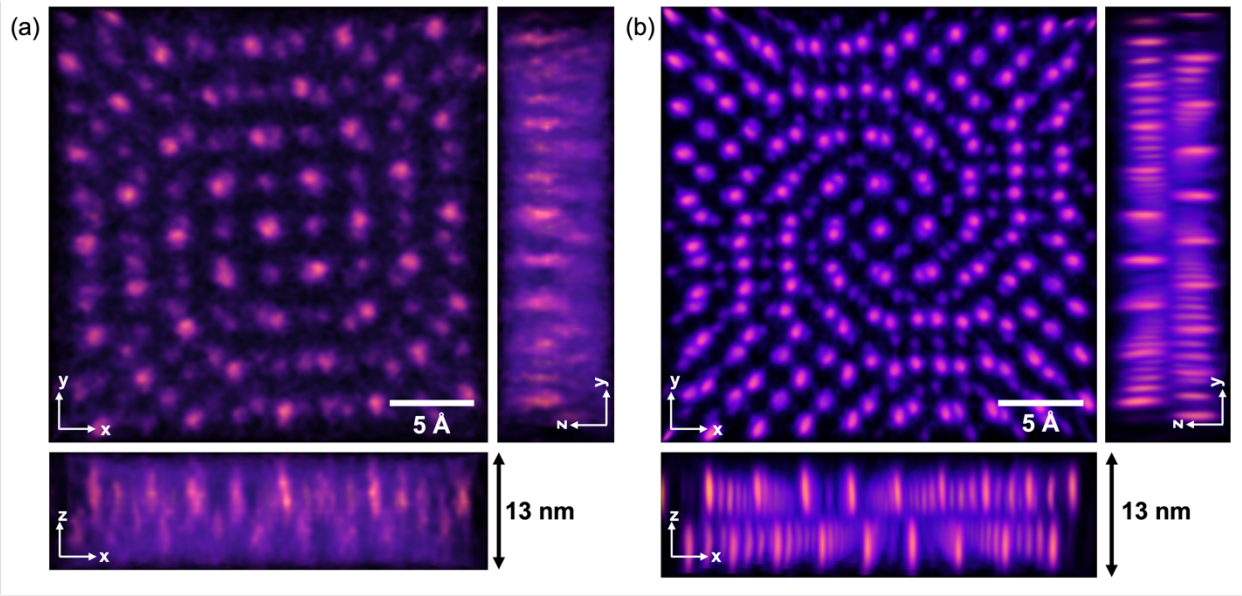

***Figure 3**. **3D visualization of the twisted, stacked bilayer** with (a) HAADF and (b) multislice ptychography. The 3D volume obtained by optical depth sectioning with HAADF is unable to resolve the gap, due to limited depth resolution and its contrast depending heavily on electron beam channeling. The 3D reconstruction with multislice ptychography shows the gap with uncoupled and undistorted atomic columns in the 2 layers, indicating the absence of structural coupling.*

In contrast, MEP solves the channeling problem, providing good lateral information transfer throughout the volume of the sample as shown in Fig. 3(b). The enhanced depth resolution of the method reveals the presence of the amorphous interlayer between the two membranes. The atomic columns in each layer are uncoupled and undistorted, indicating the absence of any interlayer structural coupling. Individual slices at different depths showing the variations in the sample structure along the beam direction are shown in Supplementary Fig. 8.

Being a computational imaging method, MEP is sensitive to the choice of reconstruction parameters, including constraints and regularizations that are applied to achieve a stable

convergence. For example, enforcing a heavy regularization in the depth direction[25,26] during MEP reconstructions can blur the interfacial gap as shown in Supplementary Fig. 9. Moreover, the enhanced mixing between adjacent slices due to such a heavy regularization can create artificial structural distortions near the interface that can propagate farther into the two layers. Therefore, cross-sectional imaging is essential to validate and constrain the interface atomic structure.

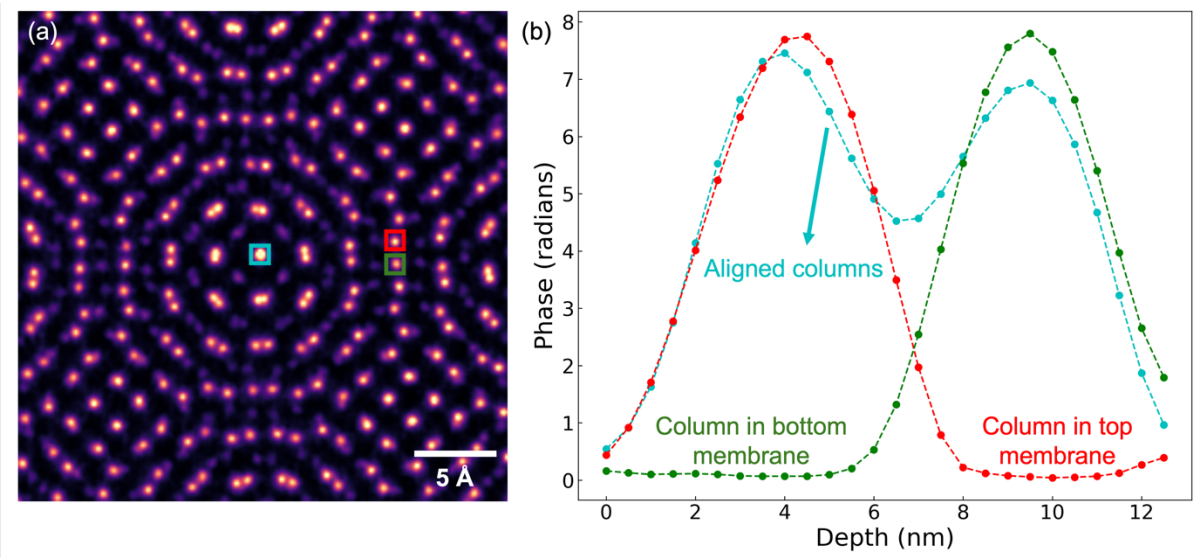

***Figure 4**. **Analysing depth resolution of MEP.** (a) Projected ptychographic reconstruction centered on an AA stacked region of the moiré pattern. Three positions are labelled, and the depth profiles of the respective atomic columns (summed over a 6x6 pixel area centered around the column) are shown in (b). The position labelled in red (green) has an atomic column present only in the top (bottom) layer as its depth profile decays rapidly in the other layer. The position labelled in cyan has columns present in both the top and bottom layers with the dip in the depth profile at the interface, indicating the presence of the gap between the two layers.*

4. Benchmarking depth resolution of MEP

The depth-sectioning capability of MEP is further explored in Fig. 4, where we plot depth profiles of individual atomic columns. Figure 4(a) shows the projected MEP reconstruction centered on an AA stacked region (local region where Sr, Ti and O columns on the 2 layers are aligned) of the moiré pattern, where three different positions are labelled. The depth profiles of the atomic columns at these labelled positions are plotted in Fig. 4(b) and clearly indicate that the column labelled in red (green) is confined to the top (bottom) membrane. The depth profile for the position marked in cyan contains atomic columns in both layers and shows a considerable dip in intensity at the interface, indicating the presence of the gap between the two membranes. The measured minima-to-peak ratio of 0.59 surpasses that needed to meet the Rayleigh resolution limit of 0.81. Moreover, summing up depth profiles from the atomic columns confined to the top and bottom membranes (red and green profiles) results in a good match with the depth profile

from the aligned columns (cyan profile) as shown in Supplementary Fig. 10, demonstrating the linearity of the imaging mode. A knife-edge analysis[32] on the red and green profiles in Fig. 4(b) gives an estimated depth resolution (difference in the depths between 90% and 10% of the maxima for the normalized phase range) of 2.31 nm and 2.46 nm respectively. We note that the knife-edge analysis will not yield meaningful results on the cyan profile in Fig. 4(b) as it does not show a plateaued minima on either side, a prerequisite for performing this analysis.

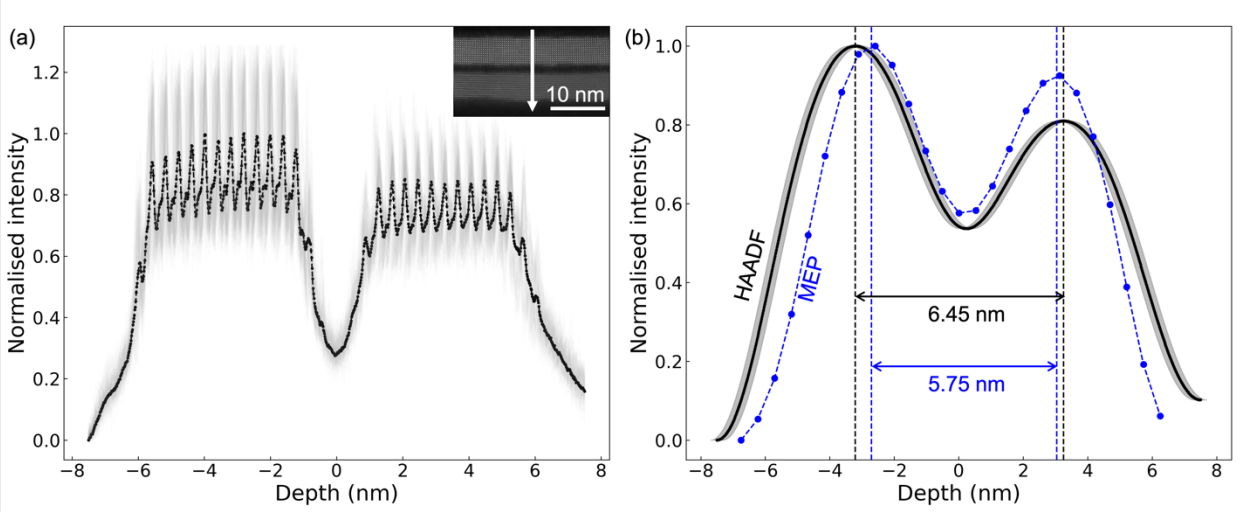

***Figure 5**. **Comparing accuracy of MEP with cross-sectional imaging.** (a) Averaged line profile through the cross-sectional HAADF image from Fig. 2(a) (shown in the inset), in bold, along with individual unit-cell-wide intensity profiles overlaid in grey with reduced opacity. (b) Gaussian-blurred HAADF cross-sectional profile plotted in black with an error band, showing the surface roughness, is compared with the MEP depth profile plotted in blue. The measured peak-to-peak distance from MEP is 11% lower than that measured from the HAADF cross-sectional line profile, indicating an underestimation of the sample thickness in MEP by 11%.*

The depth profiles obtained with MEP were also directly compared with intensity profiles from cross-sectional imaging. Figure 5(a) shows the averaged line profile across the two membranes measured from the cross-sectional HAADF image shown in the inset (same as in Fig. 2(a)). The cross-sectional image shows evidence of finite surface roughness of the membranes, with a unit cell high step visible on the bottom surface. Hence, we calculate individual line profiles with unit-cell width from the cross-sectional image and overlay them in grey color with reduced opacity to show the spread in the intensity profile due to the surface roughness. We also note that the HAADF intensity is different for the two membranes due to variations in electron channeling arising from their relative crystallographic orientations. Since the MEP depth profile has a finite depth resolution, the HAADF cross-sectional line profile is blurred to match the minima-to-peak ratio of the MEP depth profile, with the comparison shown in Fig. 5(b). The blurring of the HAADF intensity profile required a Gaussian filter with a standard deviation of 1.34 nm or a full width at 80% maximum (FW80M) of 1.8 nm, with the latter being a direct estimate of the depth-

resolution obtained with MEP. This estimate of the depth resolution surpasses the diffraction limit of 4.4 nm (depth of field given by $\frac{2\lambda}{\alpha^2}$, where semi-convergence angle (α) =30 mrad, wavelength of 300 keV electrons (λ) =1.97 pm)[38] even without accounting for the additional chromatic blur, as scattered intensity in the dark field boosts information transfer of MEP to higher frequencies (upper limit given by $\frac{2\lambda}{\theta^2}$ = 0.9 nm, where collection angle (θ) =66 mrad). Further details on how the depth resolution is influenced by dose, convergence and collection angles, and strength of the scattering species are discussed in Chen et al[26].

Comparison of the depth profiles in Fig. 5(b) indicates that MEP underestimates the overall sample extent in the depth direction by 11% as determined from peak-to-peak distance measurements. The surface roughness from the imaged area shown by means of an error band around the HAADF line profile in Fig. 5(b) is insufficient to explain this discrepancy. As the cross-sectional and plan-view images are taken at different sample regions, we also numerically estimate the surface roughness arising from step terraces of unit cell height (0.3905 nm) that could occur at the four different surfaces in the bilayer stack. Adding them in quadrature gives a net uncertainty of 0.79 nm (6%) for the sample thickness (double the peak-to-peak distance measured from the HAADF profile), also insufficient to explain the underestimation in sample thickness from the MEP depth profile. Instead, this systematic error appears to arise from the neglect of the effect of phonons in the forward scattering model currently used in ptychographic reconstruction codes. Using multislice simulations shown in Supplementary Fig. 11, we show that phonons hinder effective electron channeling along atomic columns, shifting the dynamical diffraction effects to greater sample thicknesses. Using a purely elastic model of electron diffraction to match experimental diffraction patterns that contain the effect of electron-phonon scattering results in an underestimation of sample thickness as we have observed. For a sample thickness in the range of 10-15 nm, we measure this difference in thickness for dynamical diffraction effects with and without phonons to be ~12%, an excellent match with the measured discrepancy in experiment. Addressing this discrepancy requires the inclusion of a scheme to account for the effects of phonons in the MEP forward model. While such models exist, they are quite computationally demanding[39–41].

We have shown that the presence of a moiré pattern in plan-view imaging with conventional STEM imaging methods is subject to artifacts. In the presence of a dead layer, a through-focal series with conventional STEM methods can be completely insensitive to the interfacial gap because of the channeling dominated contrast mechanism and aperture-size limited depth resolution. We further demonstrated how these limitations can be addressed with multislice electron ptychography, enabling the detection of the interfacial dead layer. However, given the nanometer-scale depth-resolution of MEP, investigation of interlayer coupling requires cross-sectional images, which can routinely achieve sub-angstrom resolution. Structural variations from surface roughness at the final nanometer of the interface can remain concealed in projection in cross-sectional HAADF imaging, making quantification of interfacial reconstructions

challenging. For example, if the cross-sectional HAADF image intensity drops at the interface and shows a darker band of contrast, this indicates that there are gaps in projection and that the two membranes are not uniformly in good atomic registry. We strongly caution against Fourier filtering of such images as it can introduce artificial atoms or atomic planes that misleadingly appear to bridge the gap as demonstrated in Supplementary Fig. 12. In such cases, 3D imaging becomes necessary to reveal details that are concealed in projection. Therefore, a combination of cross-sectional imaging with HAADF or MEP and plan-view depth-sectioning with MEP is needed to achieve a comprehensive characterization of interfacial proximity and potential structural reconstructions in these moiré structures.

5. Hybrid interface between a 2D material and oxide membrane

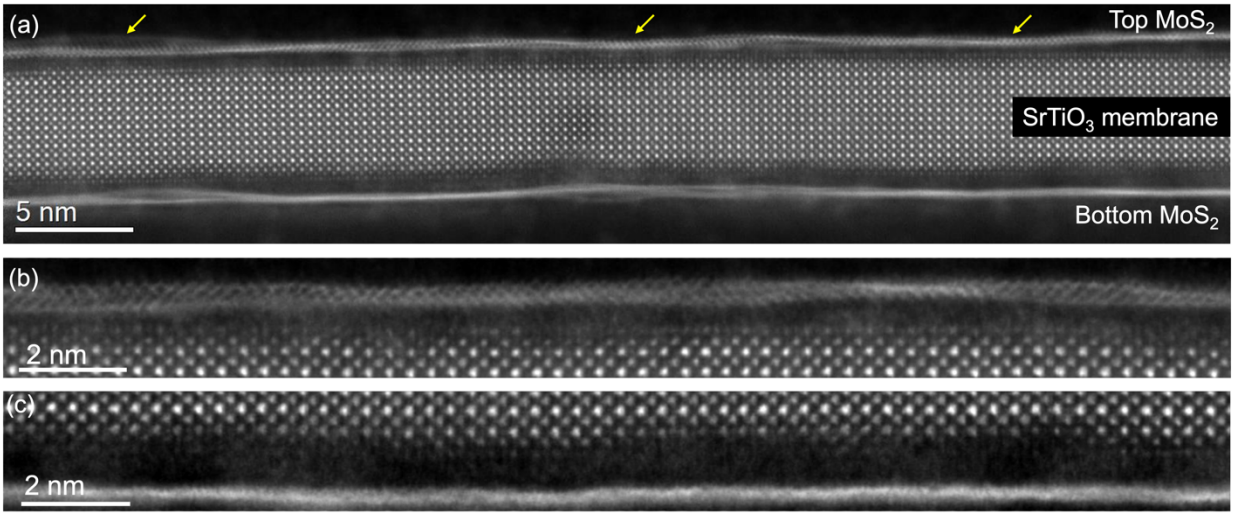

Figure 6. Hybrid 2D-3D interfaces. *(a) Cross-sectional HAADF image of MoS_2 (monolayer) / $SrTiO_3$ / MoS_2 (monolayer) heterostructure. Patches where the 2D material and oxide membrane are atomically close are marked with yellow arrows. (b, c) Magnified images of the top and bottom interfaces. MoS_2 does not conform fully to the $SrTiO_3$ membrane due to the surface roughness of the oxide membrane.*

Although our discussion above focused on a bilayer stack of oxide membranes, similar challenges also exist for interfaces between 2D materials and oxide membranes[42–44]. An example of such a mixed interface is illustrated in Fig. 6 for a MoS_2 (monolayer) / $SrTiO_3$ / MoS_2 (monolayer) heterostructure. Figure 6(a) shows a large field-of-view cross-sectional HAADF image of the heterostructure, revealing a visible gap between the layers, interspersed with small patches of atomic-scale proximity (labelled with yellow arrows). Using electron energy loss spectroscopy (EELS), we show that both top and bottom interfaces are clean with no carbon contamination layer (typically present at such interfaces if the transfer is not clean) between the 2D material and the oxide membrane, with details of the analysis shown in Supplementary Fig. 13. Magnified images of the top and bottom interfaces are shown in Fig. 6 (b, c) respectively and used to calculate an average interlayer distance (Mo plane – terminating

layer of $SrTiO_3$) of 5.59 ± 0.87 Å and 6.37 ± 1.50 Å for the top and bottom interfaces respectively. Accounting for the Mo-S interplanar distance of 1.62 Å, this measured interlayer distance (~ 4 Å) is still slightly larger than typical van-der Waals distances (2.9 Å for bulk MoS_2). Although the carbon contamination layer is eliminated, an overall interfacial gap persists as the MoS_2 monolayer cannot conform perfectly to the surface of the $SrTiO_3$ membrane.

6. Conclusion

As detailed above, there remain significant challenges and opportunities for improving the quality of interfaces in bilayer membranes. Unlike van der Waals materials which have a stable surface termination, oxide membranes often form contamination layers at their surfaces, especially on exposure to environmental factors during the liftoff or transfer processes. The surface roughness of the oxide membranes also needs to be carefully controlled to prevent interfacial coupling from occurring only at isolated patches. Meticulous sample preparation including, but not limited to, careful surface treatments, cryogenic transfer protocols, and high-temperature annealing steps, can produce atomically sharp interfaces in related material systems as demonstrated in recent reports with a twisted stack of layered high-temperature cuprate superconductors[45] (interface between exfoliated flakes of a van der Waals oxide) and an epitaxially incompatible symmetry-forbidden interface between $SrTiO_3$ and sapphire[14] (membrane-single crystal interface). As interlayer coupling in a stacked bilayer is reliant on close proximity of the two layers and is an inherent assumption in theoretical modeling of moiré materials or hybrid 2D-3D heterostructures, optimizing the interface will be key in unlocking the new physics that they may hold.

Acknowledgements

H.K., K.J.C., Y.-T.S., J.-H.K., C.L., J.P., H.Y.H., and D.A.M. acknowledge funding from the Department of Defense, Air Force Office of Scientific Research under award FA9550-18-1-0480. X.W., Y.L., and R.X. acknowledge support from the US Department of Energy, Office of Basic Energy Sciences, Division of Materials Sciences and Engineering, under Contract No. DE-AC02-76SF00515. C.-H.L. would like to thank the support from the Eric and Wendy Schmidt AI in Science Postdoctoral Fellowship, a program of Schmidt Sciences, LLC. R.X. acknowledges the support from the National Science Foundation (NSF) under award No. DMR-2442399. This work made use of the electron microscopy facility of the Platform for the Accelerated Realization, Analysis, and Discovery of Interface Materials (PARADIM), which is supported by the National Science Foundation under Cooperative Agreement No. DMR-2039380 and Cornell Center for Materials Research shared instrumentation facility with Helios FIB supported by NSF (DMR-1539918). The authors thank John Grazul, Mariena Silvestry Ramos, Steven Zeltmann, Phil Carubia, and Malcolm Thomas for technical support and maintenance of the electron microscopy facilities. The authors also thank Dr. Varun Harbola, Prof. Darrell Schlom, and Prof. Kyle Shen for insightful discussions.

References

[1] Y. Cao, V. Fatemi, S. Fang, K. Watanabe, T. Taniguchi, E. Kaxiras, P. Jarillo-Herrero, *Nature* **2018**, *556*, 43.

[2] R. Bistritzer, A. H. MacDonald, *Proceedings of the National Academy of Sciences* **2011**, *108*, 12233.

[3] E. Y. Andrei, D. K. Efetov, P. Jarillo-Herrero, A. H. MacDonald, K. F. Mak, T. Senthil, E. Tutuc, A. Yazdani, A. F. Young, *Nat Rev Mater* **2021**, *6*, 201.

[4] E. Y. Andrei, A. H. MacDonald, *Nat. Mater.* **2020**, *19*, 1265.

[5] K. F. Mak, J. Shan, *Nat. Nanotechnol.* **2022**, *17*, 686.

[6] Y. Cao, V. Fatemi, A. Demir, S. Fang, S. L. Tomarken, J. Y. Luo, J. D. Sanchez-Yamagishi, K. Watanabe, T. Taniguchi, E. Kaxiras, R. C. Ashoori, P. Jarillo-Herrero, *Nature* **2018**, *556*, 80.

[7] G. Chen, L. Jiang, S. Wu, B. Lyu, H. Li, B. L. Chittari, K. Watanabe, T. Taniguchi, Z. Shi, J. Jung, Y. Zhang, F. Wang, *Nat. Phys.* **2019**, *15*, 237.

[8] E. C. Regan, D. Wang, C. Jin, M. I. Bakti Utama, B. Gao, X. Wei, S. Zhao, W. Zhao, Z. Zhang, K. Yumigeta, M. Blei, J. D. Carlström, K. Watanabe, T. Taniguchi, S. Tongay, M. Crommie, A. Zettl, F. Wang, *Nature* **2020**, *579*, 359.

[9] Y. Xu, S. Liu, D. A. Rhodes, K. Watanabe, T. Taniguchi, J. Hone, V. Elser, K. F. Mak, J. Shan, *Nature* **2020**, *587*, 214.

[10] H. Li, S. Li, E. C. Regan, D. Wang, W. Zhao, S. Kahn, K. Yumigeta, M. Blei, T. Taniguchi, K. Watanabe, S. Tongay, A. Zettl, M. F. Crommie, F. Wang, *Nature* **2021**, *597*, 650.

[11] J. Liu, X. Dai, *Nat Rev Phys* **2021**, *3*, 367.

[12] N. Pryds, D.-S. Park, T. S. Jespersen, S. Yun, *APL Materials* **2024**, *12*, 010901.

[13] J. Shen, Z. Dong, M. Qi, Y. Zhang, C. Zhu, Z. Wu, D. Li, *ACS Appl. Mater. Interfaces* **2022**, *14*, 50386.

[14] H. Wang, V. Harbola, Y.-J. Wu, P. A. van Aken, J. Mannhart, *Advanced Materials* **2024**, *36*, 2405065.

[15] S. Lee, D. J. P. de Sousa, B. Jalan, T. Low, *Science Advances* **2024**, *10*, eadq0293.

[16] G. Sánchez-Santolino, V. Rouco, S. Puebla, H. Aramberri, V. Zamora, M. Cabero, F. A. Cuellar, C. Munuera, F. Mompean, M. Garcia-Hernandez, A. Castellanos-Gomez, J. Íñiguez, C. Leon, J. Santamaria, *Nature* **2024**, *626*, 529.

[17] H. Sha, Y. Zhang, Y. Ma, W. Li, W. Yang, J. Cui, Q. Li, H. Huang, R. Yu, *Nat Commun* **2024**, *15*, 10915.

[18] M.-S. Kim, K. Lee, R. Ishikawa, K. Song, N. A. Shahed, K.-T. Eom, M. S. Rzchowski, E. Y. Tsymbal, N. Shibata, T. Mizoguchi, C.-B. Eom, S.-Y. Choi, **2025**, DOI 10.48550/arXiv.2502.20738.

[19] D. Dimos, P. Chaudhari, J. Mannhart, F. K. LeGoues, *Phys. Rev. Lett.* **1988**, *61*, 219.

[20] H. Hilgenkamp, J. Mannhart, *Rev. Mod. Phys.* **2002**, *74*, 485.

[21] L. Fitting, S. Thiel, A. Schmehl, J. Mannhart, D. A. Muller, *Ultramicroscopy* **2006**, *106*, 1053.

[22] H. L. Xin, V. Intaraprasonk, D. A. Muller, *Applied Physics Letters* **2008**, *92*, 013125.

[23] H. L. Xin, D. A. Muller, *Journal of Electron Microscopy* **2009**, *58*, 157.

[24] A. M. Maiden, M. J. Humphry, J. M. Rodenburg, *J. Opt. Soc. Am. A, JOSAA* **2012**, *29*, 1606.

[25] Z. Chen, Y. Jiang, Y. T. Shao, M. E. Holtz, M. Odstrčil, M. Guizar-Sicairos, I. Hanke, S. Ganschow, D. G. Schlom, D. A. Muller, *Science* **2021**, *372*, 826.

[26] Z. Chen, Y.-T. Shao, S. E. Zeltmann, H. K. P., E. R. Rosenberg, C. A. Ross, Y. Jiang, D. A. Muller, **2024**, DOI 10.48550/arXiv.2407.18063.
[27] H. Kp, R. Xu, K. Patel, K. J. Crust, A. Khandelwal, C. Zhang, S. Prosandeev, H. Zhou, Y.-T. Shao, L. Bellaiche, H. Y. Hwang, D. A. Muller, *Nat. Mater.* **2025**, *24*, 1433.
[28] H. Zhang, G. Li, J. Zhang, D. Zhang, Z. Chen, X. Liu, P. Guo, Y. Zhu, C. Chen, L. Liu, X. Guo, Y. Han, *Science* **2023**, *380*, 633.
[29] H. Sha, J. Cui, J. Li, Y. Zhang, W. Yang, Y. Li, R. Yu, *Science Advances* **2023**, *9*, eadf1151.
[30] M. Zhu, M. Xu, Y. Qi, C. Gilgenbach, J. Kim, J. Zhang, B. R. Denzer, L. W. Martin, A. M. Rappe, J. M. LeBeau, **2024**, DOI 10.48550/arXiv.2408.11685.
[31] Z. Dong, Y. Zhang, C.-C. Chiu, S. Lu, J. Zhang, Y.-C. Liu, S. Liu, J.-C. Yang, P. Yu, Y. Wang, Z. Chen, *Nat Commun* **2025**, *16*, 1219.
[32] C. M. O'Leary, H. Sha, J. Zhang, C. Su, S. Kahn, H. Jiang, A. Zettl, J. Ciston, J. Miao, *Phys. Rev. Appl.* **2024**, *22*, 014016.
[33] J. M. Cowley, A. F. Moodie, *Acta Crystallographica* **1957**, *10*, 609.
[34] J. Rodenburg, A. Maiden, in *Springer Handbook of Microscopy* (Eds.: P. W. Hawkes, J. C. H. Spence), Springer International Publishing, Cham, **2019**, pp. 819–904.
[35] G. Segantini, C.-Y. Hsu, C. W. Rischau, P. Blah, M. Matthiesen, S. Gariglio, J.-M. Triscone, D. T. L. Alexander, A. D. Caviglia, *Nano Lett.* **2024**, *24*, 14191.
[36] Y. Li, C. Xiang, F. M. Chiabrera, S. Yun, H. Zhang, D. J. Kelly, R. T. Dahm, C. K. R. Kirchert, T. E. L. Cozannet, F. Trier, D. V. Christensen, T. J. Booth, S. B. Simonsen, S. Kadkhodazadeh, T. S. Jespersen, N. Pryds, *Advanced Materials* **2022**, *34*, 2203187.
[37] E. G. T. Bosch, I. Lazić, *Ultramicroscopy* **2019**, *207*, 112831.
[38] V. Intaraprasonk, H. L. Xin, D. A. Muller, *Ultramicroscopy* **2008**, *108*, 1454.
[39] B. Diederichs, Z. Herdegen, A. Strauch, F. Filbir, K. Müller-Caspary, *Nat Commun* **2024**, *15*, 101.
[40] Z. Herdegen, B. Diederichs, K. Müller-Caspary, *Phys. Rev. B* **2024**, *110*, 064102.
[41] A. Gladyshev, B. Haas, T. M. Boland, P. Rez, C. T. Koch, **2023**, DOI 10.48550/arXiv.2309.12017.
[42] J.-K. Huang, Y. Wan, J. Shi, J. Zhang, Z. Wang, W. Wang, N. Yang, Y. Liu, C.-H. Lin, X. Guan, L. Hu, Z.-L. Yang, B.-C. Huang, Y.-P. Chiu, J. Yang, V. Tung, D. Wang, K. Kalantar-Zadeh, T. Wu, X. Zu, L. Qiao, L.-J. Li, S. Li, *Nature* **2022**, *605*, 262.
[43] A. J. Yang, K. Han, K. Huang, C. Ye, W. Wen, R. Zhu, R. Zhu, J. Xu, T. Yu, P. Gao, Q. Xiong, X. Renshaw Wang, *Nat Electron* **2022**, *5*, 233.
[44] J. Choi, K. J. Crust, L. Li, K. Lee, J. Luo, J.-P. So, K. Watanabe, T. Taniguchi, H. Y. Hwang, K. F. Mak, J. Shan, G. D. Fuchs, *Nano Lett.* **2024**, *24*, 8948.
[45] S. Y. F. Zhao, X. Cui, P. A. Volkov, H. Yoo, S. Lee, J. A. Gardener, A. J. Akey, R. Engelke, Y. Ronen, R. Zhong, G. Gu, S. Plugge, T. Tummuru, M. Kim, M. Franz, J. H. Pixley, N. Poccia, P. Kim, *Science* **2023**, *382*, 1422.

Supplementary Information

Methods

$SrTiO_3$ thin-film growth

15 u.c. $SrTiO_3$ / 20 u.c. $Sr_2CaAl_2O_6$ heterostructures were synthesized on 5 × 5 mm^2 (001)-oriented single-crystalline $SrTiO_3$ substrates by pulsed laser deposition (KrF, λ = 248 nm). $SrTiO_3$ substrates were *in situ* pre-annealed at 930 °C under oxygen partial pressure $P_{O_2} = 5 \times 10^{-6}$ Torr for 30 minutes to obtain a step-and-terrace surface. The sacrificial layer $Sr_2CaAl_2O_6$ was grown at 700 °C with $P_{O_2} = 5 \times 10^{-6}$ Torr, laser fluence F = 3.12 J cm^{-2} (spot size = 2.20 mm^2) and laser repetition frequency f = 1 Hz. $SrTiO_3$ layer was grown at 700 °C with $P_{O_2} = 5 \times 10^{-6}$ Torr, F = 0.89 J cm^{-2} (spot size = 3.20 mm^2), and f = 1 Hz. A single-crystal $SrTiO_3$ target was used for the $SrTiO_3$ growth, while polycrystalline ceramic target was used for $Sr_2CaAl_2O_6$ growth.

Twisted $SrTiO_3$ membrane fabrication

The $SrTiO_3$ thin films were spin-coated with A8 950 polymethyl methacrylate (PMMA) at 3,500 r.p.m. for 60 seconds, with a ramping rate of 1,000 r.p.m. s^{-1}, achieving a thickness of approximately 1 μm. Following spin-coating, the films were cured at 135 °C for 7.5 minutes. The samples were immersed in deionized water for 6 hours to dissolve the sacrificial layer. The $SrTiO_3$ membrane were then transferred onto 200 nm-thick perforated SiN_x membranes with circular holes in diameter of 2 μm, supported by 200 μm Si frame. For improved bonding, the samples were heated at 110 °C for 10 min before being dipped into acetone and isopropanol subsequently for 10 min to dissolve the PMMA. The freestanding $SrTiO_3$ membranes on TEM grids were annealed in a tube furnace at 700 °C for 1 hour (900 °C, 3 hours for Sample 2) under ambient atmosphere. To minimize air exposure and maintain a clean interface, the second-layer $SrTiO_3$ membrane was immediately transferred onto the annealed first-layer $SrTiO_3$ with the desired twist angle. After the second transfer, the PMMA removal and anneal conditions were repeated for second $SrTiO_3$ layer to obtain a twisted $SrTiO_3$ device.

MoS_2 thin-film growth

Monolayer MoS_2 films were synthesized by metal organic chemical vapor deposition. Molybdenum hexacarbonyl (MHC) and diethyl sulfide (DES) are chosen as chemical precursors for Mo and S, respectively. They are introduced to a growth chamber in gas phase with H_2 and N_2. We use a total pressure of ~10 Torr and growth temperature of ~ 600 ºC. The flow rates of precursors are 5 sccm for MHC, 0.12 sccm for DES, 1 sccm for H_2, and 1500 sccm for N_2, which were regulated by mass flow controllers.

MoS_2 membrane fabrication

The steps for separation of van der Waals materials from their substrates were:

- Spin coating of an adhesive polymer layer of PMMA (Poly-methyl methacrylate, 495 K, 4% diluted in anisole) for 90 seconds at 4000 rpm on an as-grown monolayer MoS_2 film sitting on its growth substrate (SiO_2/Si).

- Baking 10 mins at 180ºC using a hot plate, followed by attaching a thermal release tape (TRT) manufactured by Nitto-Denko.
- TRT/PMMA/MoS_2 is then separated from the SiO_2/Si substrate via mechanical peeling without the use of any chemicals or etchants, which keeps the bottom surface of MoS_2 clean.

Fabrication of 2D material – oxide interfaces

Fabrication of vdw/non-vdW heterostructures was performed as follows. First, fabrication of $MoS_2/SrTiO_3$ heterostructure (vdW on top of non-vdW) is done by vacuum stacking, mounting TRT/PMMA/MoS_2 on the top stage holder and putting another as-grown $SrTiO_3$ film on the bottom stage of the vacuum box. The chamber was evacuated to less than 200 mTorr and the bottom stage heated to 150ºC. The top holder was lowered to make a contact between MoS_2 and the $SrTiO_3/Sr_2CaAl_2O_6/$ $SrTiO_3$ heterostructure using the z-motion linear vacuum feedthrough, keeping them in contact for 10 mins. Then the top holder was lifted with the stacked sample. After these steps, TRT/PMMA/MoS_2 is attached to the $SrTiO_3/Sr_2CaAl_2O_6/SrTiO_3$ heterostructure, forming a pristine $MoS_2/SrTiO_3$ interface. The sample is then taken out and placed in deionized water at room temperature until the sacrificial $Sr_2CaAl_2O_6$ layer is fully dissolved. Next, to make a heterostructure of $MoS_2/SrTiO_3/MoS_2$ (non-vdW on top of vdW), the TRT/PMMA/$MoS_2/SrTiO_3$ was mounted on MoS_2/SiO_2/Si and stacked in vacuum system, and then separation process of TRT/PMMA/$MoS_2/SrTiO_3/MoS_2$ from SiO_2/Si was repeated as explained above. TRT is easily removed by hot plate annealing and PMMA is removed by acetone and isopropanol to generate $MoS_2/$ $SrTiO_3/MoS_2$ hybrid heterostructures.

Scanning transmission electron microscopy (STEM)

The cross-sectional samples were prepared using a Thermo Fisher Helios G4 UX focused ion beam using the standard lift-out method. The plan-view imaging was done with the sample on a TEM grid with 2 um holes. All STEM data on the twisted bilayer oxide sample was collected using an aberration corrected Thermo Fisher Spectra X-CFEG STEM, operated at 300 kV, probe semi-convergence angle of 30 mrad and probe current of 60 pA. The collection angle for HAADF images was 62-200 mrad. DPC data was acquired on the Panther segmented detector with a collection angle of 15-55 mrad. The EDX data was acquired on a Dual-X detector with a dispersion of 5 eV and a frame time of 5.2 seconds, with 439 frames acquired in total.
Data on the $MoS_2/SrTiO_3/MoS_2$ heterostructure was acquired with an aberration-corrected FEI Titan Themis X-FEG STEM (300 keV beam energy and probe semi-convergence angle of 21.4 mrad). The EEL spectra were acquired using a 965 GIF Quantum ER spectrometer and a Gatan UltraScan scintillator-based detector.

Multislice electron ptychography (MEP)

The 4D-STEM datasets for ptychography were acquired on an EMPAD-G2 detector[1] operated at 10 kHz. The parameters used for data acquisition are scan-step size of 0.42 Å, probe overfocus of 7 nm, outer collection angle of 66 mrad, and total dose of around 2 x 10^5 electrons/Å^2.

Optimal parameters for the ptychographic reconstruction were determined using a Bayesian optimization code[2]. Initial ptychographic reconstructions were done using the maximum-likelihood algorithm[3] implemented in the fold-slice package[4,5]. The reconstructions were run for 1000 iterations, used a slice thickness of 0.5 nm, 4 probe modes, and a k_z multilayer regularization of 0.2 (set to 1 for the reconstruction shown in Supplementary Fig. 9). The results were further optimized using PtyRAD[6], an automatic differentiation based ptychographic reconstruction package including an affine transformation of the scan positions to account for non-orthogonality in the slow and fast scan directions induced from misalignment of the scan coils and sample drift. The reconstructions in PtyRAD used a z-regularization in real space equivalent to a Gaussian blur with a standard deviation of 0.5 nm, instead of the k_z-regularization used in fold-slice.
The 3D volume rendering of the MEP stack of slices and HAADF through-focal series is done using tomviz[7].

Schematic for parallax effect
Outlines for the duck and cloud used in the parallax schematic shown in Fig. 1 were first hand-drawn, followed by digitization using the OpenCV python package. Sr atoms were then placed along the outlines to create the objects used in the simulation. The multislice calculations for simulation of the diffraction patterns were carried out using the abTEM[8] simulation suite and used a beam energy of 300 keV and a probe semi-convergence angle of 30 mrad. The probe is overfocused 50 nm and 250 nm with respect to the duck and cloud respectively.

Supplementary Figures

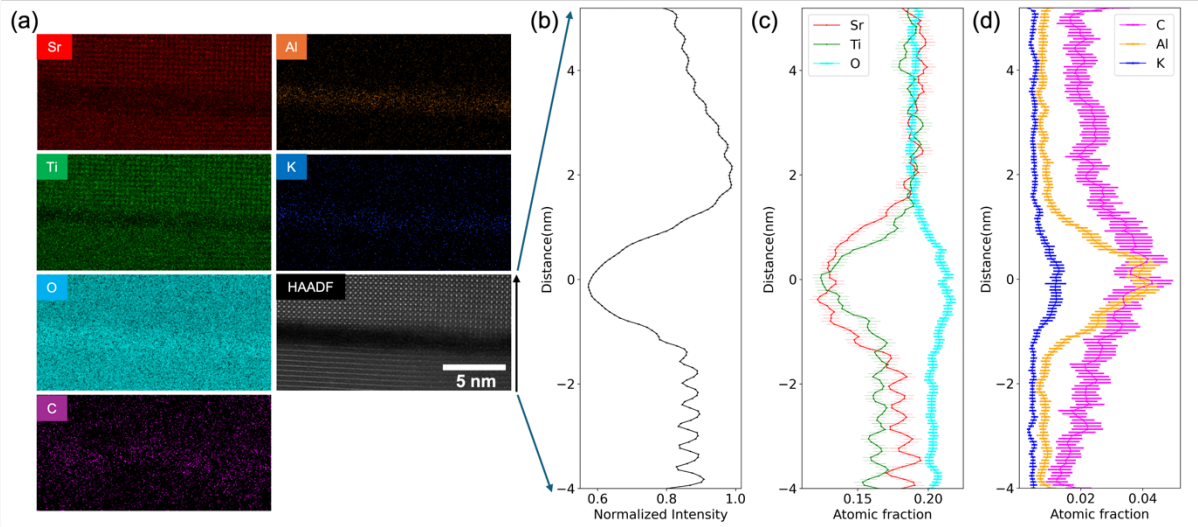

Supplementary Fig. 1 | Energy dispersive X-ray (EDX) spectroscopy on Sample 1 - cross-sectional sample of the twisted $SrTiO_3$ bilayer. (a) Elemental maps of the different elements detected in the EDX spectrum. (b-d) Line profile (averaged parallel to the dead layer) of the (b) HAADF image intensity, (c) atomic fraction of Sr, Ti, O, and (d) atomic fraction of C, Al, K. We note that the atomic fraction of O is rescaled by a factor of 1/3. The line profiles show the presence of higher amounts of C, O, Al and K in the gap region, indicating the presence of organic materials as well as trace amounts of remanent oxides from the sacrificial layer.

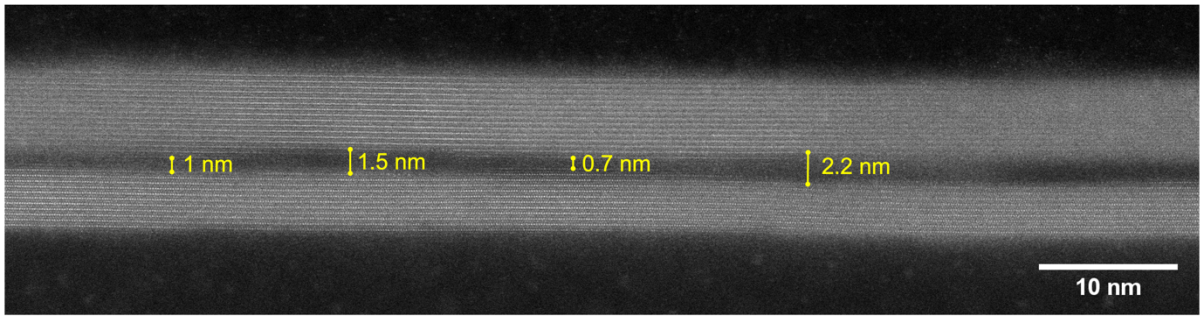

Supplementary Fig. 2 | Cross-sectional HAADF image of Sample 2 (bilayer $SrTiO_3$ membrane sample) with large variations in the extent of the interfacial gap due to the surface roughness of the top and bottom membranes.

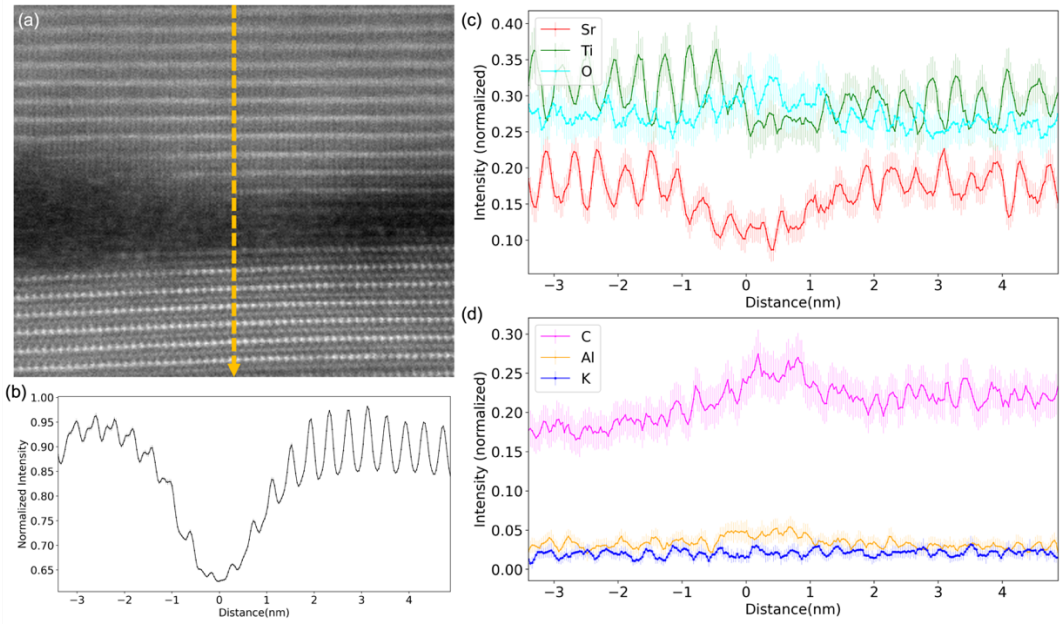

Supplementary Fig. 3 | Energy dispersive X-ray (EDX) spectroscopy on Sample 2. (a) Cross-sectional HAADF image of the bilayer. (b) Line profile of the HAADF image intensity along the yellow dotted line in (a) and averaged in the perpendicular direction. Normalized intensity of (c) Sr (L-lines), Ti (K-lines), O (K-lines), and (d) C, Al, K (K-lines for all). The normalization is such that the total counts for each data point for all elements sums up to 1. The line profiles show higher amounts of C and O in the gap region. 2D elemental maps and atomic fractions are not presented as the counts were too low for any quantification.

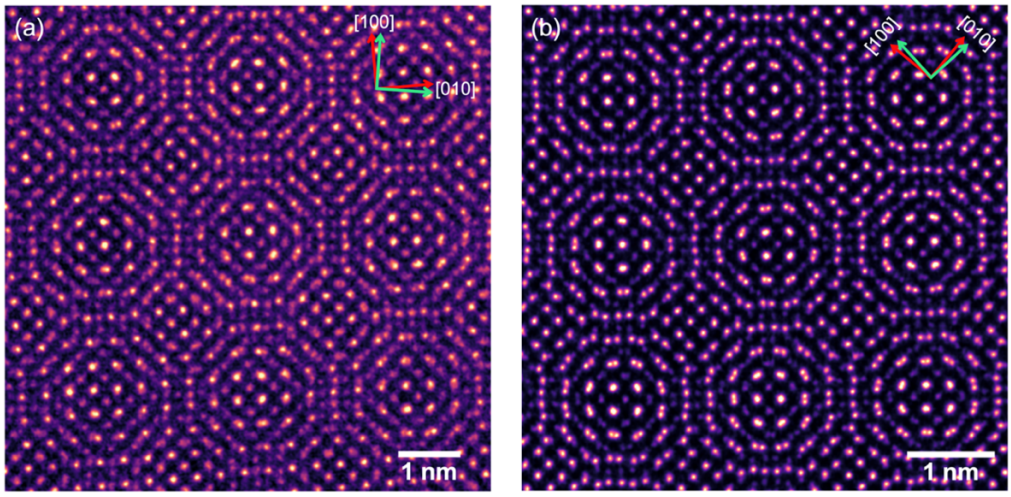

Supplementary Fig. 4 | Projected moiré patterns of Sample 1 from (a) HAADF, and (b) multislice ptychography that look visually identical, although they cover different spatial extents. The spatial extent of the field of view in the HAADF image is roughly $\sqrt{2}$ times larger and rotated by 45° with respect to the ptychographic image. The similarity in the patterns after the above geometrical transformations results from the different scaling of the image contrast with atomic number and is illustrated in detail in the following Supplementary figures.

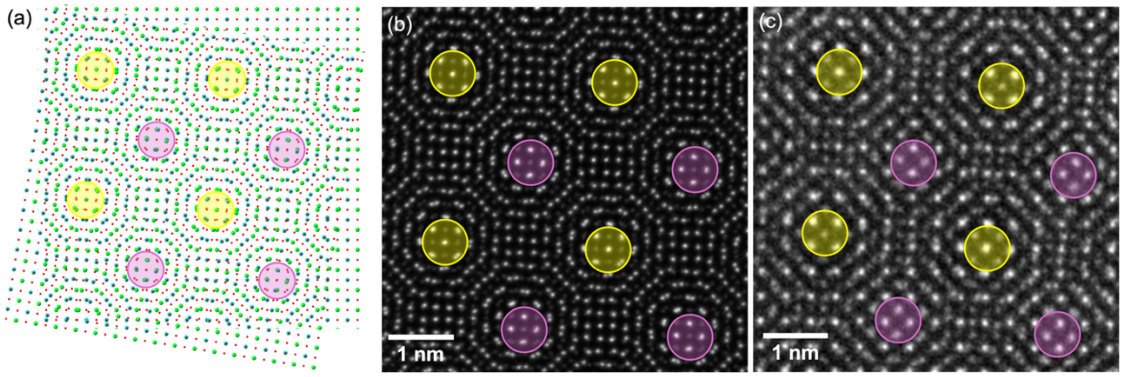

Supplementary Fig. 5 | (a) Schematic of a moire pattern created by a 9° twist angle between 2 $SrTiO_3$ layers with AA (AB) stacked regions marked with yellow (plum) color. (b) Projected multislice ptychographic reconstruction of the twisted bilayer $SrTiO_3$ sample (Sample 1) displaying a similar pattern. Due to the similar contrast of the Sr columns and Ti-O columns in multislice ptychography, the AA stacked regions centered at the A-site or the B-site look visually similar. (c) Projected HAADF image of the twisted bilayer $SrTiO_3$ sample (Sample 1) – the moire pattern looks visually different from the schematic because the oxygen atoms are not present. The AA stacked regions centered at the A-site and B-site can be distinguished due to the stronger contrast of the Sr column with respect to the Ti column.

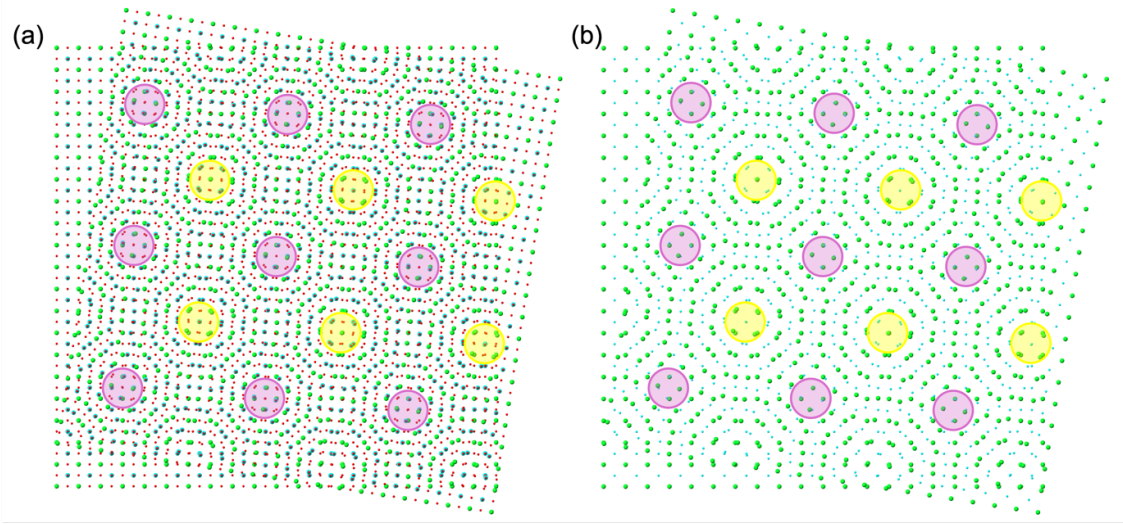

Supplementary Fig. 6 | Overlay of projected crystal structures of $SrTiO_3$ with a relative twist angle of 9° to mimic the moiré pattern in (a) multislice ptychography, and (b) HAADF. The weak Z contrast of multislice ptychography results in similar contrast from the Sr and Ti-O columns, and weaker contrast from the O columns, reflecting the choice of the size of the atoms in (a). In (b), the oxygen atoms are completely removed, and the atoms in the Ti-O column have half the size as the Sr atoms to mimic the contrast of HAADF imaging. The two patterns visually appear different due to the different sizes assigned to the atoms, a distinction that is also evident in the experimental moiré patterns.

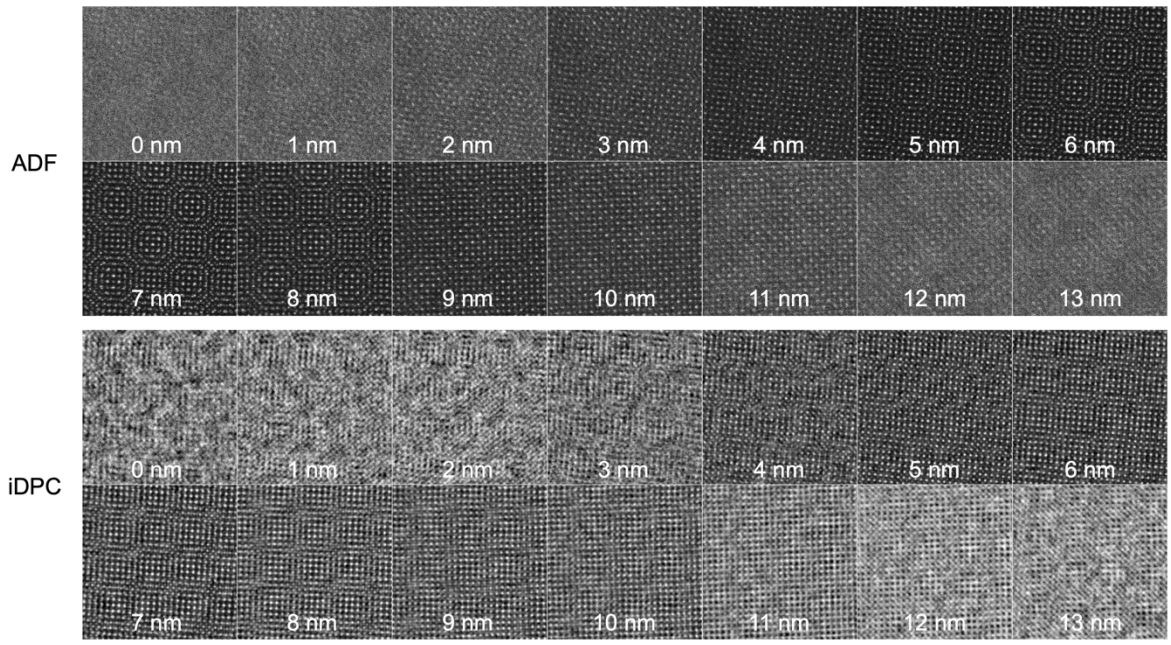

Supplementary Fig. 7 | Montage of the images acquired with ADF and iDPC imaging in an optical through-focal series for Sample 1. The field of view shown in the above images is around 7.36 nm x 7.36 nm. Both ADF and iDPC images show good contrast only for a limited range of defocus.

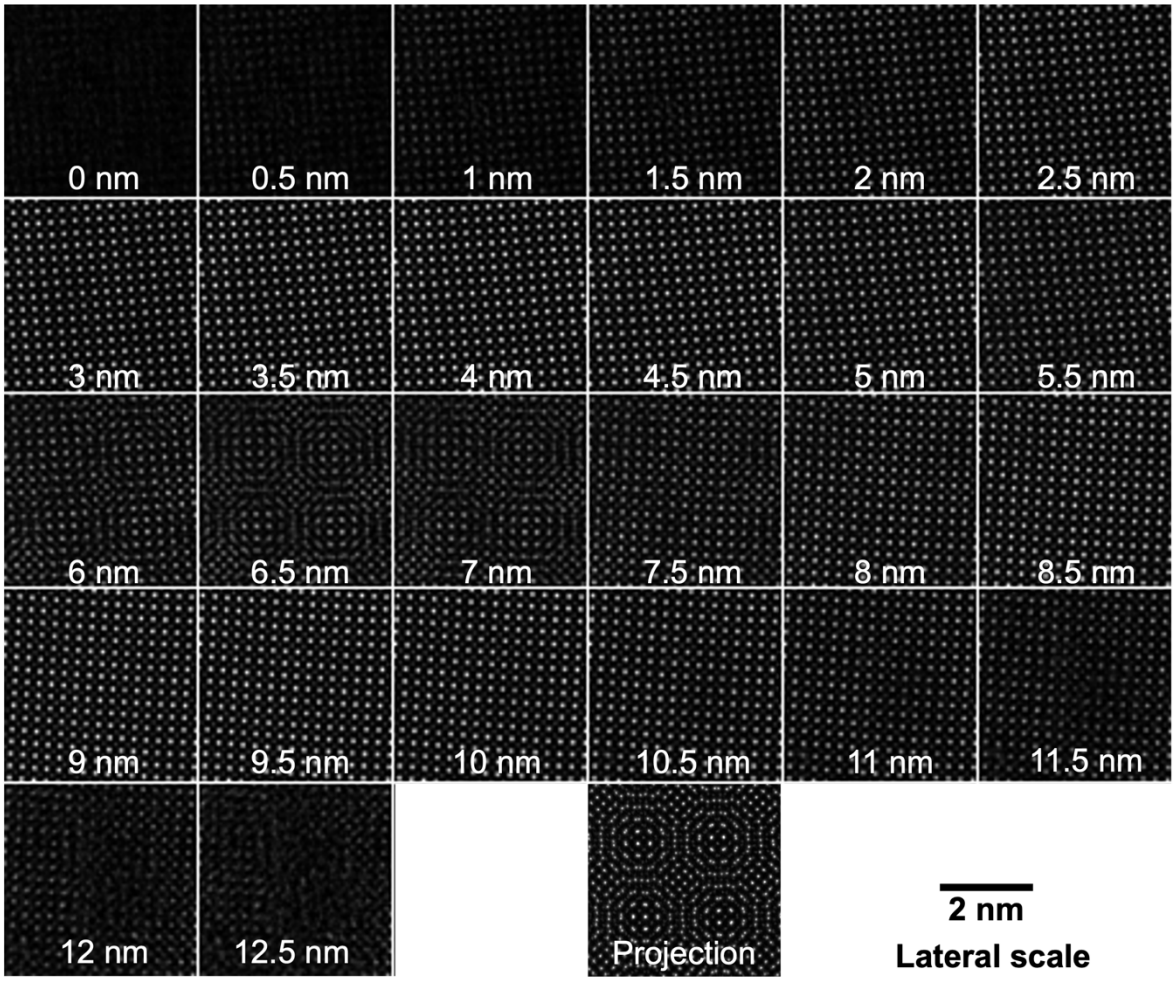

Supplementary Fig. 8 | Montage of different slices in the multislice ptychographic reconstruction of Sample 1 showing the sample structure at different depths in the beam direction.

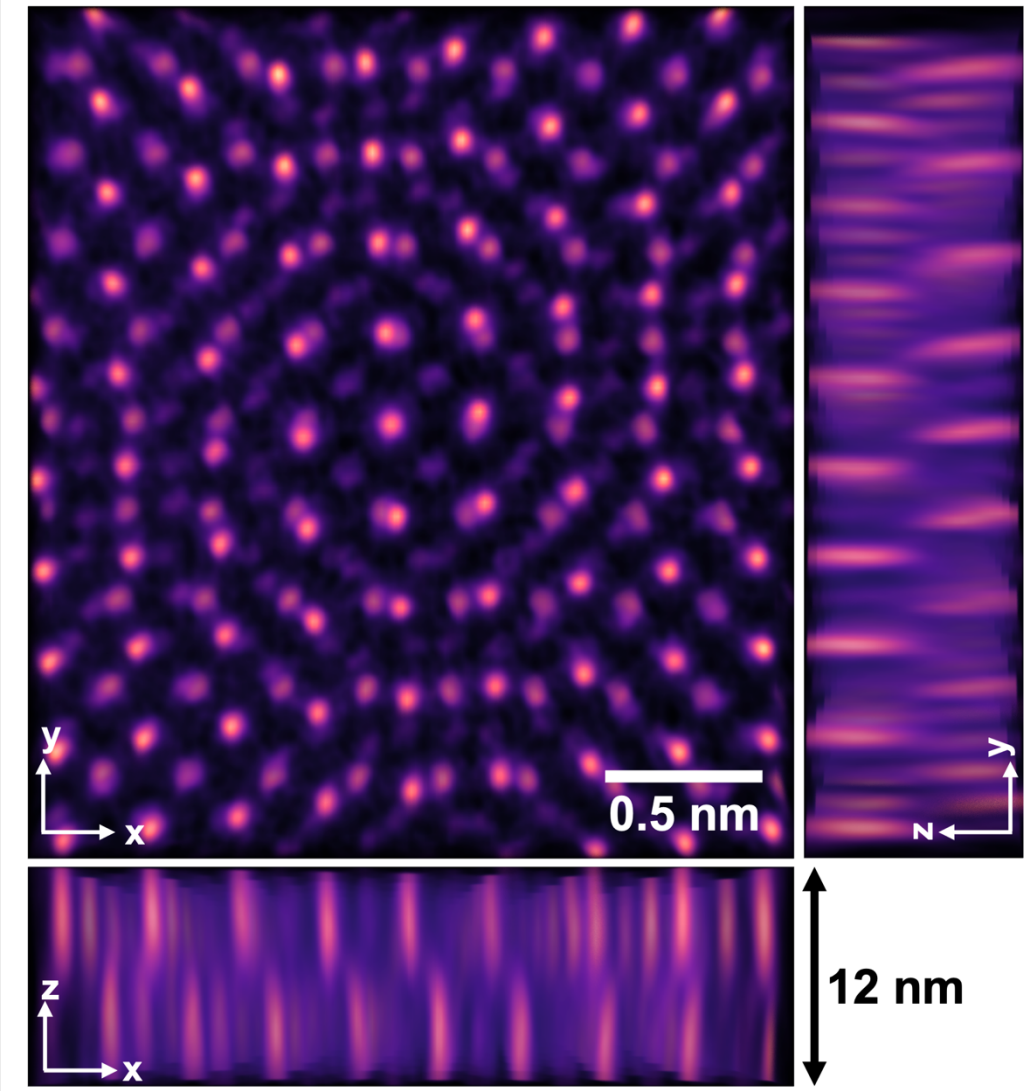

Supplementary Fig. 9 | 3D visualization of the twisted, stacked bilayer (Sample 1) with multislice ptychography using a heavy regularization (kz multilayer regularization of 1 in fold-slice) for slices along the z-axis. The presence of the dead layer is less obvious and the strong computational coupling between the different slices can create artificial distortions near the interface.

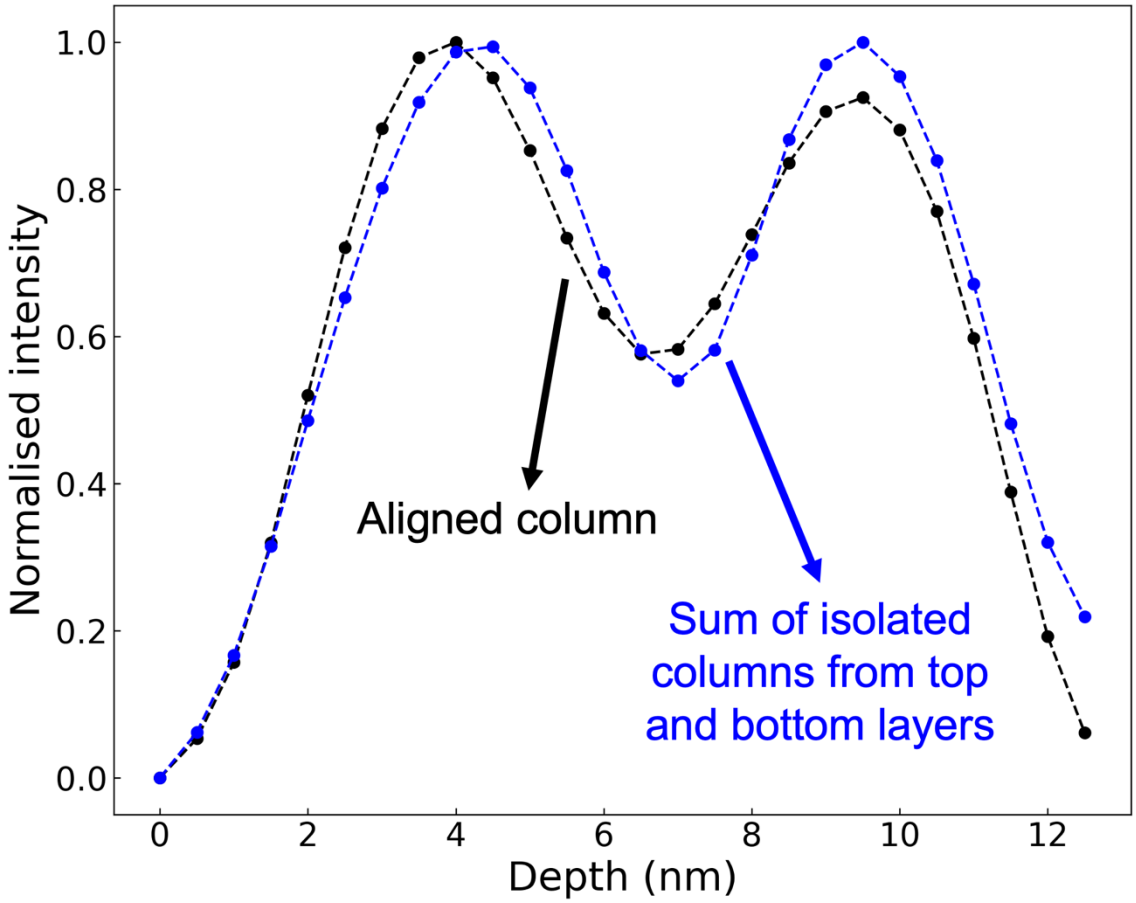

Supplementary Fig. 10 | The depth profile shown in black is obtained by summing up two depth profiles corresponding to two separate atomic columns that are confined in the top membrane and the bottom membrane respectively. The depth profile shown in blue is measured along an atomic column that is aligned in both membranes. The close match between the two resulting depth profiles indicates the linearity of MEP as an imaging mode.

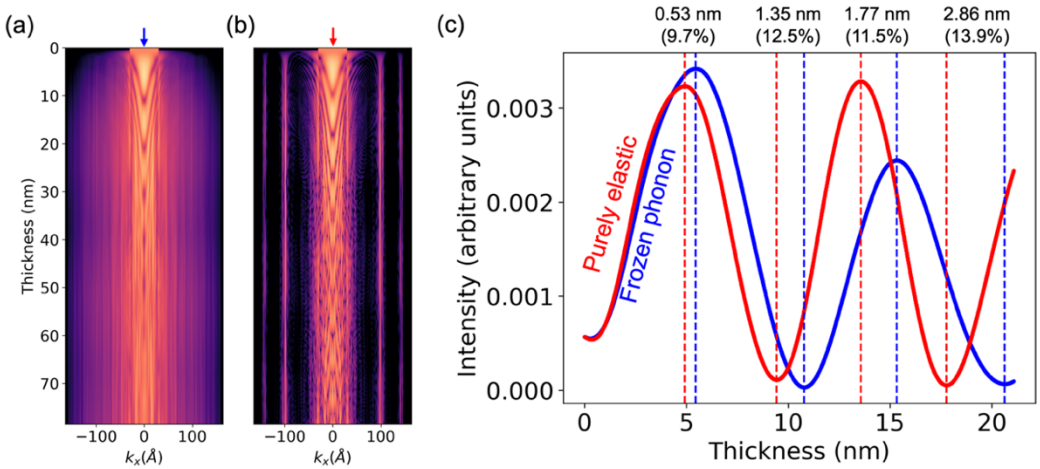

Supplementary Fig. 11 | Comparison of channelling effects in diffraction patterns simulated with and without accounting for the effect of phonons with the probe focused on top of a Sr column in $SrTiO_3$. (a, b) The intensity profile through the diffraction pattern in the [100] direction is plotted as a function of thickness (a) accounting for electron-phonon scattering through the frozen phonon approximation[9] and (b) with a purely elastic model of diffraction. (c) Intensity variations of the center of the diffraction pattern marked with blue and red arrows in (a, b) plotted as a function of thickness. The addition of phonon scattering delays the onset of channelling induced minima and maxima in the intensity profile with respect to a purely elastic scattering model. For sample thickness in the range of 10-15 nm relevant to this study, this offset in thickness between the purely elastic model and the frozen phonon model is around 12%, consistent with the observed underestimation of thickness in the MEP reconstruction of experimental data. The diffraction patterns are simulated using abTEM[8] package with a probe semi-convergence angle of 30 mrad and beam energy of 300 keV.

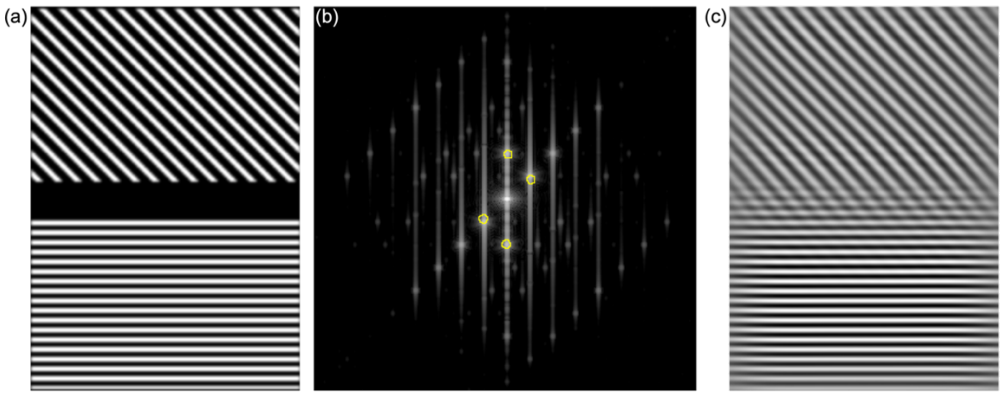

Supplementary Fig. 12 | Illustration of how Fourier filtering can introduce artificial atomic planes. (a) An image with two sets of parallel lines with a gap in between made to mimic a gapped heterostructure. (b) Fourier transform of the image in (a) with yellow circles around the first order peaks that are used as masks to create the Fourier-filtered image in (c). The Fourier-filtered image shows artificial planes in the gap due to the real-space coarsening from the finite size of the mask in Fourier space.

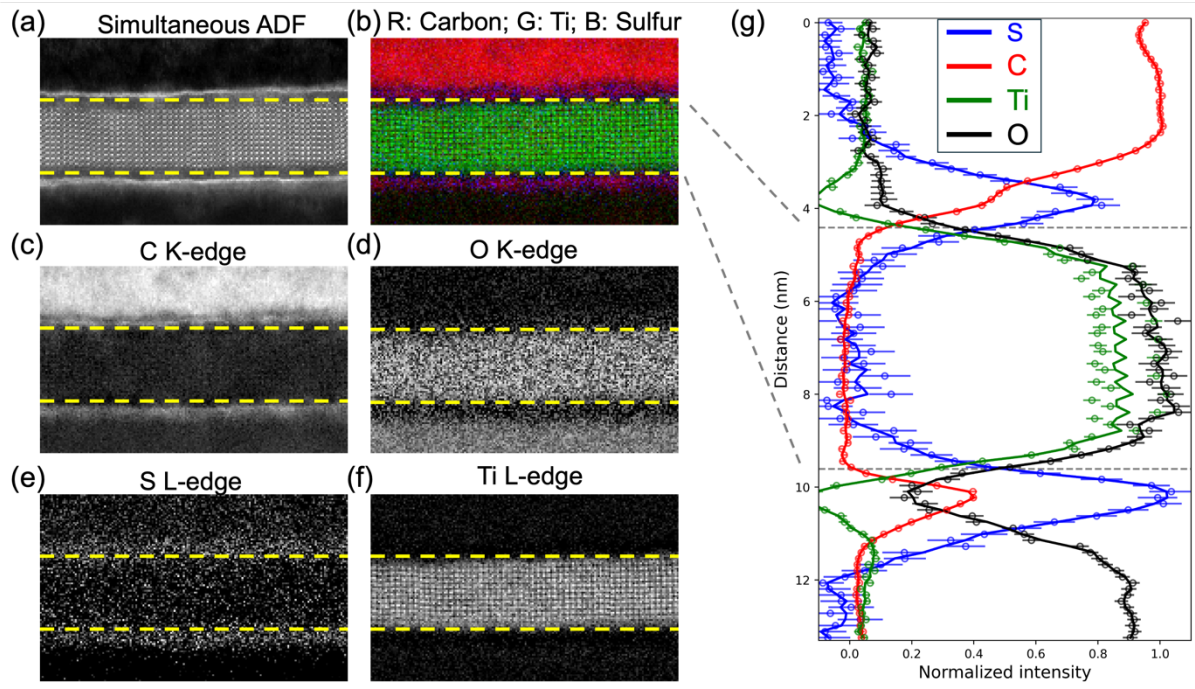

Supplementary Fig. 13 | (a) ADF image of the MoS_2 (monolayer) / $SrTiO_3$ / MoS_2 (monolayer) heterostructure taken simultaneously with the EEL spectra. (b) Composite elemental map of carbon (red), titanium (green) and sulphur (blue) generated from (c, e, f). (c-f) Elemental maps of carbon, oxygen, sulphur, and titanium respectively calculated from the EEL spectra. (g) Averaged line profile across the interface calculated from the elemental maps in (c-f). The absence of a prominent carbon peak between the sulphur peaks from MoS_2 and the Ti peak from $SrTiO_3$ indicates that there is no interfacial contamination layer.

References

[1] H. T. Philipp, M. W. Tate, K. S. Shanks, L. Mele, M. Peemen, P. Dona, R. Hartong, G. Van Veen, Y. T. Shao, Z. Chen, J. Thom-Levy, D. A. Muller, S. M. Gruner, *Microsc. Microanal.* **2022**, *28*, 425.

[2] C. Zhang, Y.-T. Shao, Z. Baraissov, C. J. Duncan, A. Hanuka, A. L. Edelen, J. M. Maxson, D. A. Muller, *Microsc. Microanal.* **2022**, *28*, 3146.

[3] P. Thibault, M. Guizar-Sicairos, *New J. Phys.* **2012**, *14*, 063004.

[4] Z. Chen, Y. Jiang, Y. T. Shao, M. E. Holtz, M. Odstrčil, M. Guizar-Sicairos, I. Hanke, S. Ganschow, D. G. Schlom, D. A. Muller, *Science* **2021**, *372*, 826.

[5] K. Wakonig, H. C. Stadler, M. Odstrcil, E. H. R. Tsai, A. DIaz, M. Holler, I. Usov, J. Raabe, A. Menzel, M. Guizar-Sicairos, *Urnissn1600-5767* **2020**, *53*, 574.

[6] C.-H. Lee, S. E. Zeltmann, D. Yoon, D. Ma, D. A. Muller, *Microsc. Microanal.* **2025**, *31*, ozaf070.

[7] J. Schwartz, C. Harris, J. Pietryga, H. Zheng, P. Kumar, A. Visheratina, N. A. Kotov, B. Major, P. Avery, P. Ercius, U. Ayachit, B. Geveci, D. A. Muller, A. Genova, Y. Jiang, M. Hanwell, R. Hovden, *Nat. Commun.* **2022**, *13*, 4458.

[8] J. Madsen, T. Susi, *Open Res. Eur.* **2021**, *1*, 24.

[9] R. F. Loane, P. Xu, J. Silcox, *Acta Crystallogr. A* **1991**, *47*, 267.